Received: 13 March 2022 | Revised: 3 June 2022 | Accepted: 26 June 2022

DOI: 10.1111/jace.18648

Journal of the American Ceramic Society

RESEARCH ARTICLE

Syntheses, characterization, magnetic, and electrochemical properties of perovskite-type $NdFeO_3$ and $NdCoO_3$ nanofibers

Quanli Hu[1] | **Bin Yue**[2] | **Wang Su**[1] | **Daotong Yang**[1] | **Yin Wang**[1] | **Xiangting Dong**[2] | **Jinghai Liu**[1]

[1]Nano Innovation Institute (NII), Inner Mongolia Key Lab of Carbon Nanomaterials, College of Chemistry and Materials Science, Inner Mongolia Minzu University, Tongliao, China

[2]Key Lab of Applied Chemistry and Nanotechnology at Universities of Jilin Province, School of Materials Science and Engineering, Changchun University of Science and Technology, Changchun, China

Correspondence
Quanli Hu and Jinghai Liu, Nano Innovation Institute (NII), Inner Mongolia Key Lab of Carbon Nanomaterials, College of Chemistry and Materials Science, Inner Mongolia Minzu University, Tongliao 028-000, China.
Email: huquanly@hotmail.com and jhliu2008@sinano.ac.cn

Xiangting Dong, Key Lab of Applied Chemistry and Nanotechnology at Universities of Jilin Province, School of Materials Science and Engineering, Changchun University of Science and Technology, Changchun 130-022, China.
Email: xtdong@cust.edu.cn

Funding information
Doctoral Scientific Research Foundation of Inner Mongolia Minzu University, Grant/Award Numbers: BS437, BS456; Research Project of Colleges and Universities in Inner Mongolia Autonomous Region, Grant/Award Number: NJZZ22461; National Natural Science Foundation of China, Grant/Award Numbers: 21961024, 21961025, 22161036; Incentive Funding from the Nano Innovation Institute of Inner Mongolia Minzu University, Grant/Award Number: MDK2019014; Inner Mongolia Autonomous Region

Abstract

In this work, perovskite-type $NdFeO_3$ and $NdCoO_3$ nanofibers (NFs) were synthesized, and the magnetic and electrochemical characteristics of the two samples were investigated. The $NdFeO_3$ NFs showed ferromagnetic performance at 298 K and paramagnetic characteristics at low temperatures, whereas the $NdCoO_3$ NFs showed paramagnetic behavior. The $NdFeO_3$ and $NdCoO_3$ electrodes exhibited favorable electrochemical performance in supercapacitors and Li-ion batteries. Therefore, this study demonstrated the potential applications of $NdFeO_3$ and $NdCoO_3$ NFs in the field of condensed matter physics and energy storage devices.

KEYWORDS
lithium-ion battery, magnetic, nanofiber, neodymium, perovskite, supercapacitors

Quanli Hu and Bin Yue contributed equally to this work.

Science & Technology Planning Project for Applied Technology Research and Development, Grant/Award Number: 2019GG261

1 | INTRODUCTION

Neodymium-based perovskite oxides, such as $NdFeO_3$ and $NdCoO_3$, have attracted the attention of researchers due to their fascinating physical and chemical properties.[1–5] $NdFeO_3$ and $NdCoO_3$ materials with significant applications have been intensively studied for solid oxide fuel cells, sensors, catalysts, and data storage devices.[6–10] In addition, the tolerance factors of $NdFeO_3$ and $NdCoO_3$ have shown to be 0.8677 and 0.8828, respectively, indicating that they possess stable perovskite structures.[11] Ferrite is a common magnetic material that has been widely studied in previous research.[12–17] The magnetic properties of $Bi_{25}FeO_{39}$ ferrite have been investigated, and at 5–300 K the effective magnetic moment of the Fe^{3+} ion has been found to be 5.82 μ_B.[12] The crystal structure evolutions of $BiFeO_3$–$BaTiO_3$ compounds have also been demonstrated, and this research has provided a remarkable strategy for the development of new functional materials.[13] The structures and magnetic properties of M-type hexaferrites ($BaFe_{12-x}Ti_xO_{19}$ and $SrFe_{12-x}In_xO_{19}$) have also been illustrated.[14,15] The crystal structure and ferroelectric properties of $SrFe_{11.9}In_{0.1}O_{19}$ have been investigated, and the relationship between the crystal structure and ferroelectric properties has been elucidated.[16] In addition, the temperature effect on the structure and magnetic properties of $SrFe_{10.8}In_{1.2}O_{19}$ has been elaborated.[17] Thus, the doping concentration, crystal structure, and temperature have shown a positive effect on the magnetic properties. As a typical orthoferrite material, $NdFeO_3$ exhibits interesting sensing and magnetic properties, as well as excellent gas sensing properties for acetone and CO_2 with high selectivity, great sensitivity, advanced responsiveness, and good reliability.[1,7] $NdFeO_3$ has two magnetic sublattices of Nd^{3+} and Fe^{3+}, and the interactions between Nd^{3+}–Nd^{3+}, Nd^{3+}–Fe^{3+}, and Fe^{3+}–Fe^{3+} result in intriguing magnetic phenomena.[3,18] As a representative cobaltite, $NdCoO_3$ has shown remarkable sensing properties for CO and propane with interesting magnetic properties and different valence states of cobalt in high-, intermedia-, and low-spin states.[5,19] The rapid development of mobile communication technology has created microwave devices with more functionalities, and the dielectric contribution and magnetic behavior have shown to play a significant role in microwave devices.[20] Therefore, it is very important to study the magnetic properties of materials. Perovskites, such as $La_{1-x}Ba_xMnO_{3-x/2}$ and $La_{1-x}Sr_xMnO_{3-x/2}$, have shown remarkable magnetic properties.[21,22] The outstanding sensing properties of $NdFeO_3$ and $NdCoO_3$ have been mainly attributed to the advantages of perovskite structures with dodecahedral coordinated Nd^{3+} and octahedral coordinated Fe^{3+}/Co^{3+}.[1,5] In addition, the high redox abilities of transition metals were found to greatly facilitate the Faradic redox reaction. Research on the electrochemical behaviors of $NdFeO_3$ and $NdCoO_3$ would be beneficial for expanding their applications in supercapacitors and lithium-ion (Li-ion) batteries. However, the electrochemical behaviors of $NdFeO_3$ and $NdCoO_3$ have rarely been investigated.

Supercapacitors and Li-ion batteries are the two major energy storage devices,[23,24] and a crucial component of supercapacitors and Li-ion batteries is the electrode material. Generally, $NdFeO_3$ and $NdCoO_3$ materials can be fabricated by coprecipitation, combustion, and sol–gel methods.[1,2,9,10,25] In addition, Ba–Sr hexaferrites can be fabricated by a solid-state reaction approach.[26] Interestingly, a green and eco-friendly method for synthesizing $BaFe_{12}O_{19}$ nanoparticles by using *Acorus calamus* has been reported.[27] Nevertheless, the morphologies of these fabricated samples will be highly aggregated, hindering the Faradic redox reaction in supercapacitor electrodes and reducing contact area in Li-ion batteries. The nanofibrous structure offers attractive merits, such as a high length-diameter ratio and abundant active sites.[28] Electrospinning technology has also shown to be a common method for fabricating nanofibers (NF)-like materials with high efficiency, high yield, and high quality.[29] Therefore, the electrochemical properties of electrospun $NdFeO_3$ and $NdCoO_3$ NFs were adequately investigated in this work.

In this research, we described the preparation of $NdFeO_3$ and $NdCoO_3$ NFs with a uniformly orthorhombic perovskite structure by electrospinning and calcination approaches. Then, the magnetic and electrochemical properties of the $NdFeO_3$ and $NdCoO_3$ NFs were investigated. The $NdFeO_3$ NFs possessed concurrent ferromagnetic and paramagnetic characteristics, whereas the $NdCoO_3$ NFs exhibited paramagnetic behavior. The $NdFeO_3$ and $NdCoO_3$ NFs also showed favorable electrochemical performances as pseudocapacitor electrodes and Li-ion battery anodes. To the best of our knowledge, few reports have investigated the electrochemical characteristics of $NdFeO_3$ and $NdCoO_3$ NFs as supercapacitor electrodes

and Li-ion battery anodes. Therefore, this research intended to clarify the electrochemical properties of $NdFeO_3$ and $NdCoO_3$ NFs and develop a new application domain, namely, the energy storage area. Magnetic analyses were used to identify the magnetic behaviors of $NdFeO_3$ and $NdCoO_3$ NFs, such as the Curie constants, Curie temperatures, effective magnetic moments, and magnetic transition phenomena. Therefore, this research offered an alternative route for synthesizing perovskite type $NdFeO_3$ and $NdCoO_3$ NFs with remarkable magnetic and electrochemical performances.

2 | EXPERIMENTAL PROCEDURES

Analytical grade reagents were used in this research, where the $NdFeO_3$ and $NdCoO_3$ NFs were prepared via electrospinning and calcination. The precursor solutions were prepared by adding $Nd(NO_3)_3{\cdot}6H_2O$ (2 mmol), metal acetate (iron acetate (FeAc), cobalt acetate tetrahydrate ($CoAc{\cdot}4H_2O$), 2 mmol), and polyvinylpyrrolidone (PVP, $M_w \approx 1300\,000$, 1 g) into *N*,*N*-dimethylformamide (DMF, 9 ml) under strong stirring overnight. The detailed electrospinning and calcination processes are presented in the Supporting Information section.

The thermostabilities of the precursors were analyzed by thermogravimetric analysis (TGA). The crystal structures, microstructure, morphology, elemental compositions, and chemical states of the $NdFeO_3$ and $NdCoO_3$ NFs were measured by X-ray diffraction (XRD) patterns, a scanning electron microscope (SEM), a transmission electron microscope (TEM) with energy-dispersive X-ray spectroscopy, and X-ray photoelectron spectroscopy (XPS), respectively.

The magnetic properties of the $NdFeO_3$ and $NdCoO_3$ NFs were demonstrated via a vibrating sample magnetometer (SQUID VSM), whereas the reciprocal susceptibility curves were replotted by the temperature dependence of the magnetization curves in zero field cool mode, where the temperature ranged from 2 to 300 K, and the applied magnetic field was 100 Oe. The field dependence of the magnetization (*M*–*H*) curves for the $NdFeO_3$ and $NdCoO_3$ samples was performed at 5, 50, and 298 K under the zero-field cooling condition.

The electrochemical performances of the $NdFeO_3$ and $NdCoO_3$ NFs as supercapacitor electrodes were investigated by an electrochemical workstation in a standard three-electrode system. The electrodes were fabricated by pressing the mixture of $NdFeO_3$/$NdCoO_3$ NFs, acetylene black, and polytetrafluoroethylene with a weight ratio of 80:10:10 on pretreated nickel foams, where the weight of the electrode material was 2.5–4 mg, and the electrolyte consisted of 3 M KOH and 0.02 M $K_3Fe(CN)_6$ solution. As Li-ion battery anodes, the electrochemical behaviors of the $NdFeO_3$ and $NdCoO_3$ NFs were studied at 30°C by a battery analyzer. The abovementioned slurry was roll-pressed on Cu foil to fabricate the Li-ion battery anodes, where the weight of the anode material was 1 mg. The 2032-type coin cells were fabricated in an Ar-filled glove box with $NdFeO_3$ ($NdCoO_3$) as the anode, lithium foil as the counter electrode, and 1 mol L^{-1} $LiPF_6$ as the electrolyte solution.

3 | RESULTS AND DISCUSSION

The thermostabilities of the $Nd(NO_3)_3$–FeAc/PVP and $Nd(NO_3)_3$–CoAc/PVP precursors were studied by TGA as shown in Figure S1. The crystal structures of the fabricated $NdFeO_3$ and $NdCoO_3$ were identified by the Rietveld refinement XRD patterns in the 2θ range from 10° to 80° as displayed in Figure 1. It was evident that the refined diffraction pattern of $NdFeO_3$ matched well with the JCPDS card (88-0477), indicating a pure orthorhombic perovskite structure with a *Pnma* (62) space group,[30] whereas the sharp and highly intense diffraction peak was indexed to the (1 2 1) plane. The refined diffraction pattern of $NdCoO_3$ was in excellent agreement with the JCPDS card (89-0551), suggesting an orthorhombic perovskite structure with a *Pnma* (62) space group.[9,31] The most intense peak was located on the (1 2 1) plane. No apparent impurity phase was observed in the XRD patterns, revealing the high phase purity of the $NdFeO_3$ and $NdCoO_3$ NFs. The relatively sharp and highly intense diffraction peaks manifested the favorable crystallinity of the $NdFeO_3$ and $NdCoO_3$ NFs. The fitting lattice parameters of the $NdFeO_3$ and $NdCoO_3$ NFs are listed in Table S1, whereas the positional details of the $NdFeO_3$ and $NdCoO_3$ NFs are shown in Table S2.

The SEM images of the precursors, $NdFeO_3$ NFs, and $NdCoO_3$ NFs are presented in Figure S2, whereas the TEM images of the $NdFeO_3$ and $NdCoO_3$ NFs are shown in Figure 2A,D. The $NdFeO_3$ and $NdCoO_3$ NFs exhibited distinct nanofibrous structures with a high length-diameter ratio, and the diameters of $NdFeO_3$ and $NdCoO_3$ were 364 and 256 nm, respectively. Moreover, the TEM images revealed that the NFs were composed of abundant small nanoparticles that were connected compactly. According to the high-resolution TEM images (Figure 2B,E), the lattice fringe with an interplanar spacing of 0.392 nm signified the (1 0 1) plane of $NdFeO_3$, whereas 0.331 nm implied the (1 1 1) plane of $NdCoO_3$. The elemental mapping images are shown in Figure 2C,F validated the homogeneous distribution of Nd, Fe/Co, and O elements in the $NdFeO_3$/$NdCoO_3$ NFs.

Figure 3 presents the XPS spectra of $NdFeO_3$ and $NdCoO_3$, whereas the high-resolution XPS spectra of Nd 3d are listed in Figure 3A,D. The two strong peaks at 982 and 1004 eV were ascribed to Nd $3d_{5/2}$ and Nd $3d_{3/2}$,

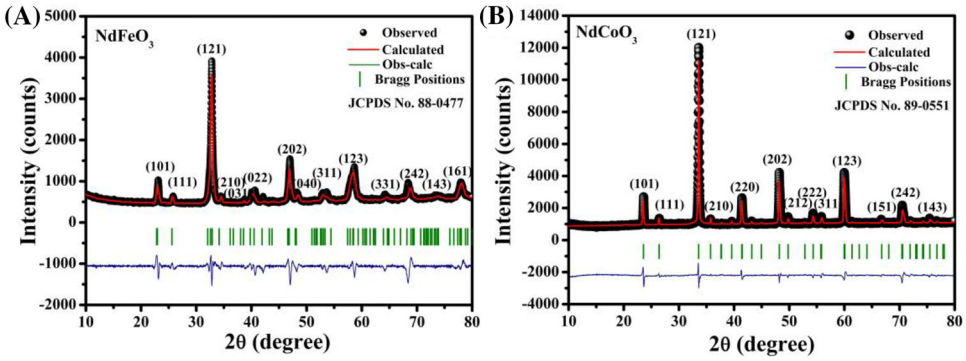

FIGURE 1 Rietveld refined X-ray diffraction (XRD) patterns of the (A) $NdFeO_3$ and (B) $NdCoO_3$ nanofibers (NFs)

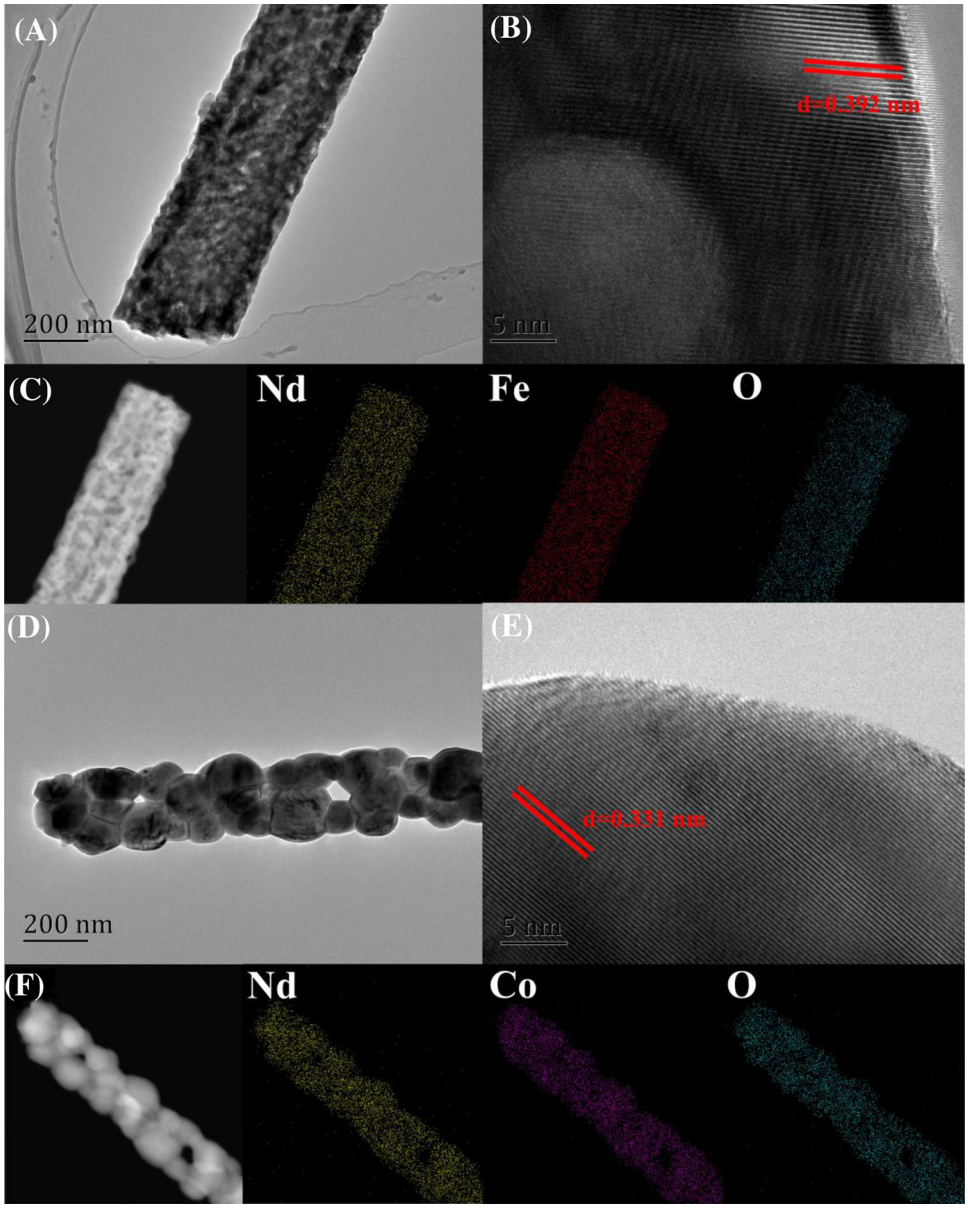

FIGURE 2 (A) Transmission electron microscope (TEM) image, (B) high-resolution TEM (HRTEM) image, (C) HAADF-STEM (high angle annular dark field scanning transmission electron microscope) image, and corresponding elemental mapping images of Nd, Fe, and O in the $NdFeO_3$ nanofiber (NF); (D) TEM image, (E) HRTEM image, (F) HAADF-STEM image, and corresponding elemental mapping images of Nd, Co, and O in the $NdCoO_3$ NF

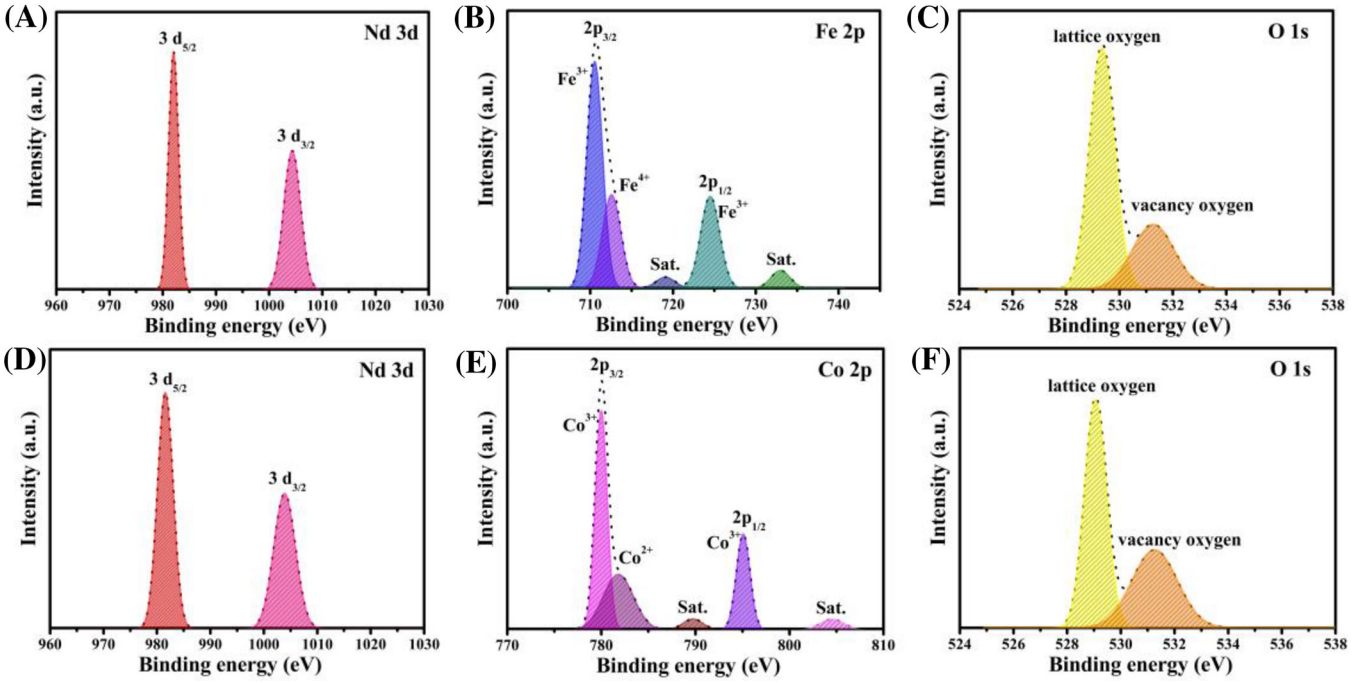

FIGURE 3 X-ray photoelectron spectroscopy (XPS) spectra of (A) Nd 3d, (B) Fe 2p, and (C) O 1s for the $NdFeO_3$ nanofibers (NFs); (D) Nd 3d, (E) Co 2p, and (F) O 1s for the $NdCoO_3$ NFs

respectively, indicating the existence of Nd^{3+}.[32] In the Fe 2p spectrum (Figure 3B), five clear peaks were located at 710.6, 712.6, 719.1, 724.5, and 733.0 eV. The peaks at 710.6 and 712.6 eV, as well as 724.5 eV corresponded to Fe $2p_{3/2}$ and Fe $2p_{1/2}$, respectively, whereas concomitant satellite peaks were located at 719.1 and 733.0 eV. This demonstrated that the valence states of Fe were +3 and +4.[33–35] In the Co 2p spectrum (Figure 3E), the peaks at 780.0 and 781.8 eV were indexed to Co $2p_{3/2}$, signifying the coexistence of Co^{3+} and Co^{2+}. The peak at 795.1 eV was ascribed to Co $2p_{1/2}$, which manifested the existence of Co^{3+}.[36] According to the O 1s spectra (Figure 3C,F), the peak at 529 eV originated from the ordered lattice oxygen ions, and 531 eV was derived from the oxygen vacancies.[36,37] The relative percentage concentrations of oxygen vacancies for the $NdFeO_3$ and $NdCoO_3$ NFs were 31% and 41%, respectively. It has been reported that the oxygen vacancies of electrode materials will positively influence electrochemical performance, and numerous oxygen vacancies will favor the adsorption of electrolyte ions, boosting the energy storage reactions.[36] Moreover, the relative percentage concentrations of Fe^{3+} and Co^{3+} for the $NdFeO_3$ and $NdCoO_3$ NFs are 84.3% and 70.2%, respectively. This implied that the main valence states of Fe and Co were +3.

The XRD patterns proved that the $NdFeO_3$ and $NdCoO_3$ NFs had orthorhombic perovskite structures, and the SEM and TEM images confirmed the NF-like morphologies of $NdFeO_3$ and $NdCoO_3$. The chemical states of Nd^{3+} and Fe^{3+}(Co^{3+}) were identified by XPS analyses. Therefore, the abovementioned characterizations confirmed the successful formation of perovskite-type $NdFeO_3$ and $NdCoO_3$ NFs.

The magnetic properties of the $NdFeO_3$ and $NdCoO_3$ NFs were investigated by VSM. The temperature dependences of the reciprocal magnetic susceptibility of the $NdFeO_3$ and $NdCoO_3$ NFs are shown in Figure 4A,C, indicating that inverse magnetic susceptibility ($1/\chi$) was gradually reduced with decreasing temperature. At 300 K, the magnetic susceptibilities (χ) of the $NdFeO_3$ and $NdCoO_3$ NFs were 3.434×10^{-5} and 4.356×10^{-5} emu Oe^{-1} g^{-1}, respectively; thus, the contribution of Nd^{3+} magnetic moments was obvious. The dependences of $NdFeO_3$ and $NdCoO_3$ obeyed the Curie–Weiss law ($\chi = C/(T - \theta_p)$) in the intermediate temperature region (100–280 and 90–255 K). C signifies the Curie constant, and θ_p indicates the Curie temperature. Therefore, based on the Curie–Weiss law, the values of C and θ_p were calculated and shown in Table S3. In addition, μ_{eff} (cal) consisted of the calculated effective magnetic moment values of $NdFeO_3$ and $NdCoO_3$. The deviation from the Curie–Weiss law in the low-temperature region was possibly attributed to the crystal field effect, whereas the high-temperature region possibly resulted from the thermally excited states of Fe^{3+} and Co^{3+} ions.[3,38] The total magnetic susceptibility of $NdFeO_3$ and $NdCoO_3$ could be described as the sum of the inequivalent magnetic subsystems, namely, the Nd ions and Fe/Co ions.[3,4] The theoretical effective magnetic moment of Nd^{3+} was 3.62 μ_B,[4] whereas the

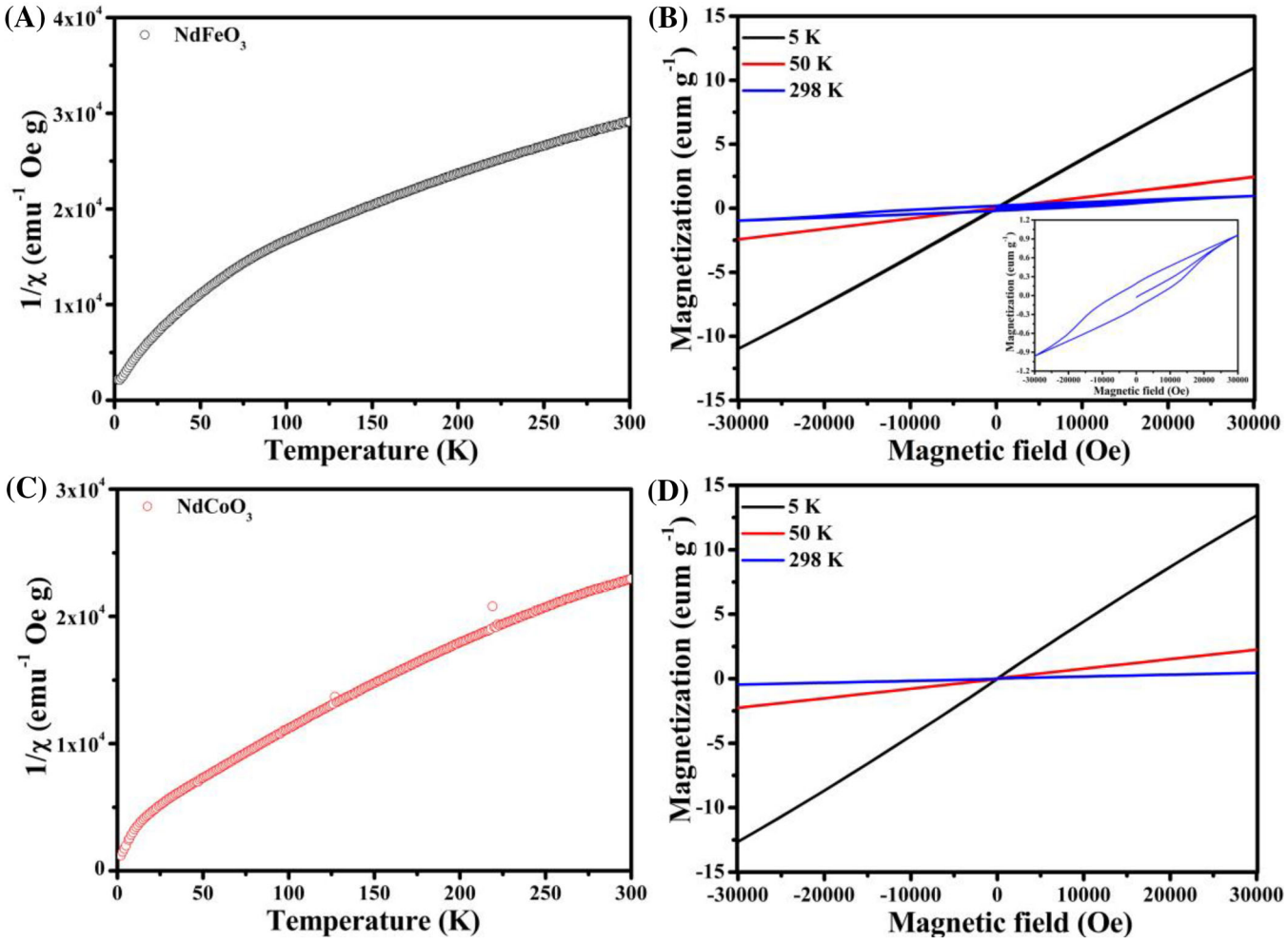

FIGURE 4 Reciprocal susceptibility for the (A) $NdFeO_3$ nanofibers (NFs) and (C) $NdCoO_3$ NFs at 100 Oe; magnetic hysteresis loops of the (B) $NdFeO_3$ NFs and (D) $NdCoO_3$ NFs at 5, 50, and 298 K. The inset shows the magnetic hysteresis loops of the $NdFeO_3$ NFs at 298 K.

theoretical effective magnetic moments of Fe^{3+} and Co^{3+} were 5.92[12] and 0.93 μ_B,[19] respectively. The *M–H* curves are shown in Figure 4B,D. $NdFeO_3$ possessed Nd^{3+} and Fe^{3+} magnetic sublattices with magnetic vectors antiparallel to each other. For $NdFeO_3$, the noncollinear antiferromagnetic state in the Fe^{3+} subsystem mainly contributed to weak ferromagnetic behavior at high temperatures, and the Nd^{3+} subsystem mostly led to the antiferromagnetic phase at low temperatures.[18] At 5 and 50 K, the *M–H* curves of $NdFeO_3$ showed no hysteresis loop, which was largely attributable to the existence of the magnetization compensation point.[3,18] Accordingly, the non-saturating hysteresis loop and weak ferromagnetic state of the $NdFeO_3$ NFs at 298 K were mainly ascribable to the noncollinear antiferromagnetic state in the Fe^{3+} subsystem,[18] where the remnant magnetization (M_r) of the $NdFeO_3$ NFs at 298 K was 0.19 emu g^{-1}. In addition, the coercivity (H_c) was 6245 Oe. $NdCoO_3$ possessed Nd^{3+} and Co^{3+} magnetic sublattices. The thermally excited Co^{3+} sublattice gave rise to a paramagnetic state[4], and the Co ions (Co^{2+}, Co^{3+}, and Co^{4+}) were located in different (high, intermedia, and low) spin states.[19] The magnetic interaction in $NdCoO_3$ involved a nonmagnetic oxygen ion; thus Co^{3+}–O^{2-}–Co^{4+} and Co^{3+}–O^{2-}–Co^{3+} led to ferromagnetic and antiferromagnetic states, respectively.[19] The magnetic state of $NdCoO_3$ originated from the Co ions in a low spin state, which switched to paramagnetism when the temperature was above 100 K.[9] In a perovskite structure, Nd^{3+} was in a low-symmetrical ligand situation, and the field was inclined to split Nd^{3+}.[4] However, the *M–H* curves of $NdCoO_3$ exhibited paramagnetic-like behavior with no hysteresis loop, which was greatly ascribed to the change of electron orbitals, derived from energy competition where the exchange energy overcame the crystal field splitting for 3d electrons in the tilted CoO_6 octahedron.[9] According to previous reports, the ac resistivity and the real part of permittivity would decrease with increasing frequency.[20,39] In addition, the chemical compositions and structure played a significant role in the material properties,[12,14] where electron hopping between

Fe^{2+} and Fe^{3+} facilitated the reduction in ac resistivity.[39] Previous reports have shown that oxygen content will highly influence the magnetic states.[40,41] The magnetic state transitions of $La_{0.5}Ca_{0.5}MnO_{3-\gamma}$ appeared from the antiferromagnetic to ferromagnetic state, from the ferromagnetic to spin-glass state, and from the spin-glass to the ununiform ferromagnetic state with different γ values.[40] It has been reported that the material size could influence the magnetic properties, such as the Curie temperature and coercivity.[30,42,43] According to the Scherrer formula, the calculated crystallite sizes of the $NdFeO_3$ and $NdCoO_3$ NFs were 81 and 178 nm, respectively. Thus, $NdFeO_3$ with a small size showed high coercivity, which was attributed to the existing defects and the combined effect of magnetization curling and buckling.[30] In addition, the $NdFeO_3$ NFs exhibited ferromagnetic performance at 298 K and paramagnetic characteristics at low temperatures, whereas the $NdCoO_3$ NFs showed paramagnetic behavior. Subsequently, the magnetic properties of the $NdFeO_3$ and $NdCoO_3$ NFs were investigated, and the electrochemical characteristics were given in the following sections.

The electrochemical behaviors of the $NdFeO_3$ and $NdCoO_3$ NFs as supercapacitor electrodes were studied, and *CV* analyses were performed at a scan rate from 1 to 100 mV s^{-1} and the potential from 0 to 0.5 V. According to Figure 5A,B, the obvious redox peaks indicated the representative pseudocapacitive behaviors of the $NdFeO_3$ and $NdCoO_3$ NFs electrodes, and the redox reactions have originated from $Fe^{2+} \leftrightarrow Fe^{3+}$ ($Co^{2+} \leftrightarrow Co^{3+}$) and $Fe(CN)_6^{4-} \leftrightarrow Fe(CN)_6^{3-}$. *CV* curves with no obvious shape deformation with elevating scan rates manifested the favorable reversibility and stability of $NdFeO_3$ and $NdCoO_3$. Table S4 lists the calculated specific capacitances based on Figure 5A,B, where at 1 mV s^{-1}, the $NdFeO_3$ and $NdCoO_3$ electrodes showed the specific capacitance values of 179.5 and 101.2 F g^{-1}, respectively. In addition, a low scan rate indicated that the electrolyte ions had sufficient time to migrate to the active materials and involve in the electrochemical reactions at the electrode, thus obtaining high capacitance.[44] The power law is used to investigate the charge storage mechanism, and the equation could be expressed by

$$i = av^b \quad (1)$$

where a and b signify variable values, i indicates the peak current, and v represents the scan rate. In addition, the b value was located between 0.5 and 1, where a b value of 0.5 signified a battery property by a diffusion-controlled process, whereas Equation (1) demonstrated a capacitive behavior by a surface-controlled process.[45–47] As depicted in Figure S5a,b, the b values of $NdFeO_3$ and $NdCoO_3$ were close to 0.5, suggesting that the charge storage mechanism was dominated by a diffusion-controlled process. The GCD curves of the $NdFeO_3$ and $NdCoO_3$ electrodes are presented in Figure 5C,D, which further confirmed the pseudocapacitive properties of $NdFeO_3$ and $NdCoO_3$. Table S5 shows the specific capacitances of $NdFeO_3$ and $NdCoO_3$ at different current densities, where at 1 A g^{-1}, the specific capacitances of $NdFeO_3$ and $NdCoO_3$ NFs were 186.8 and 94.5 F g^{-1}, respectively. The coulombic efficiency and available redox reaction active sites of $NdFeO_3$ and $NdCoO_3$ NFs were calculated and are listed in Table S6. The electrochemical interfacial properties of $NdFeO_3$ and $NdCoO_3$ were measured by EIS from 10 mHz to 100 kHz with an AC signal amplitude of 5 mV at an open circuit potential. According to Figure S6, the Nyquist plots consisted of an oblique line in the low frequency region, indicating rapid diffusion between the electrode and electrolyte interface, and the absence of a semicircle in the high frequency region implied low interfacial Faradic charge transfer resistance at the interface of the $NdFeO_3$ ($NdCoO_3$)/electrolyte. The cycling stabilities of $NdFeO_3$ and $NdCoO_3$ NFs are shown in Figure S7.

The electrochemical properties of the $NdFeO_3$ and $NdCoO_3$ NFs as Li-ion battery anodes were also researched. As presented in Figure 6A, for the first cycle, the broad peak at 0.07–0.1 V was attributed to the reaction of the $NdFeO_3$ electrode with the electrolyte and the development of a solid electrolyte interface film, where the peak at 1.85 V was mainly ascribed to the transition from Fe^{2+} to Fe^{3+}.[48] For the second cycle, the oxidation peak of the $NdFeO_3$ NFs moved slightly to 1.91 V, and the curve showed a wide peak at 0.42 V, whereas the broad peak from 0.6 to 1.0 V was due to the conversion of Fe^{3+} to Fe^0,[49] and the peak at 0.42 V could be derived from the valence changed of Nd. For the fifth cycle, the redox peaks changed slightly, proving the good stability of the $NdFeO_3$ NFs. Figure 6B displays the *CV* curves of the $NdCoO_3$ NFs, where the peak at 0.42 V during the first discharge process could be attributed to Nd valence changes, similar to Figure 6A. Two weak peaks located at 1.78 and 0.68 V during the first charge process originated from the multistage electrochemical lithiation process from Co to Co^{3+}.[50] In the subsequent process, the disappearance of the peak at 0.42 V and the attenuation of the oxidation peak indicated the fading of the redox reaction in the $NdCoO_3$ NFs. The reactions of the $NdFeO_3$ and $NdCoO_3$ NFs during the charge–discharge process could be described by the following formulas, and we noticed that the irreversible decay of the capacity in $NdCoO_3$ resulted from the nonreversible reactions of (4) during

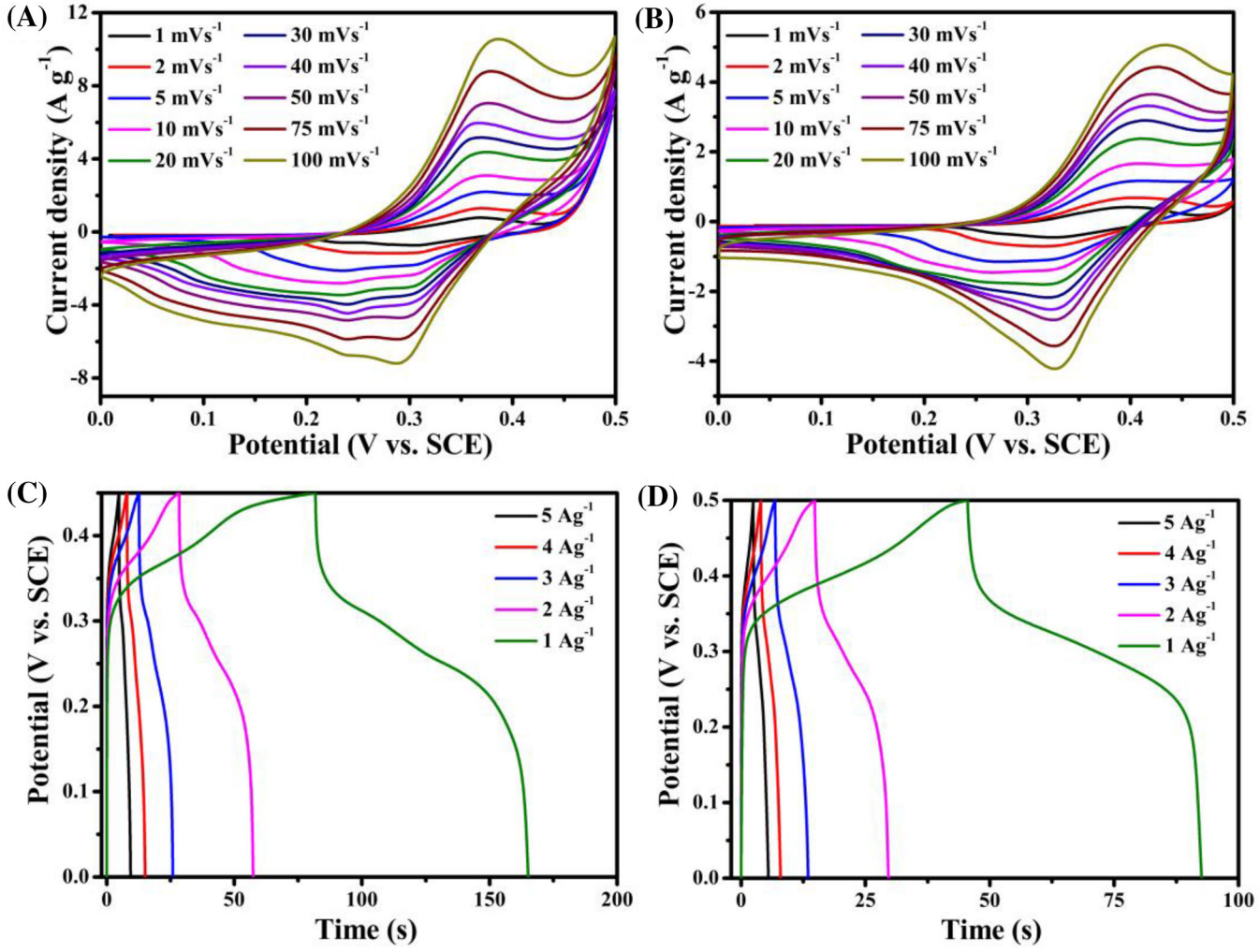

FIGURE 5 *CV* curves of the (A) $NdFeO_3$ nanofiber (NF) and (B) $NdCoO_3$ NF electrodes at different scan rates; GCD profiles of the (C) $NdFeO_3$ NFs and (D) $NdCoO_3$ NFs at different current densities

repeated cycling:

$$NdFeO_3 + 4Li^+ + 4e^- \leftrightarrow Nd + FeO + 2Li_2O \quad (2)$$

$$FeO + 2Li^+ + 2e^- \leftrightarrow Fe + Li_2O \quad (3)$$

$$NdCoO_3 + 4Li^+ + 4e^- \rightarrow Nd + CoO + 2Li_2O \quad (4)$$

$$CoO + 2Li^+ + 2e^- \leftrightarrow Co + Li_2O \quad (5)$$

The stability behaviors of the $NdFeO_3$ and $NdCoO_3$ NFs are presented in Figure 6C. $NdFeO_3$ NFs showed a gradual upward trend, and their capacity increased from 337 to 531 mA h g^{-1} after 400 cycles, which was due to the activation process of the electrode material.[51] The capacity finally stabilized at 467 mA h g^{-1} at the 500th cycle. The capacity of $NdCoO_3$ NFs declined during the first 100 cycles and then subsequently increased. This phenomenon was attributed to the formation of the polymer/gel-like film and electrode lithiation.[52] Finally, after 500 cycles the capacity was 280 mA h g^{-1}, and the capacity retention rates of $NdFeO_3$ and $NdCoO_3$ were 116.75% and 127.85%, respectively, proving the favorable stability of these materials as Li-ion battery anodes. As shown in Figure 6D, the rate performances of the $NdFeO_3$ and $NdCoO_3$ NFs were measured at different current densities. The $NdFeO_3$ and $NdCoO_3$ anodes exhibited capacities of 114 and 11 mA h g^{-1} under 2000 mA g^{-1}. And the capacities recovered to 243 and 105 mA h g^{-1} when the current density went back to 200 mA g^{-1}. EIS was implemented to further explore the Li^+ diffusion inside these anode materials. Figure 6E shows the Nyquist plots of $NdFeO_3$ and $NdCoO_3$, where the inset shows the equivalent circuit, and the R_{ct} values of $NdFeO_3$ and $NdCoO_3$ were 44.03 and 56.64 Ω, respectively. The Bode plots are shown in Figure 6F according to the fitting of the value of $\omega^{-0.5}$ and $|Z|$. In addition, the exchange current density ($i°$) and the diffusion coefficient of Li^+ (D)

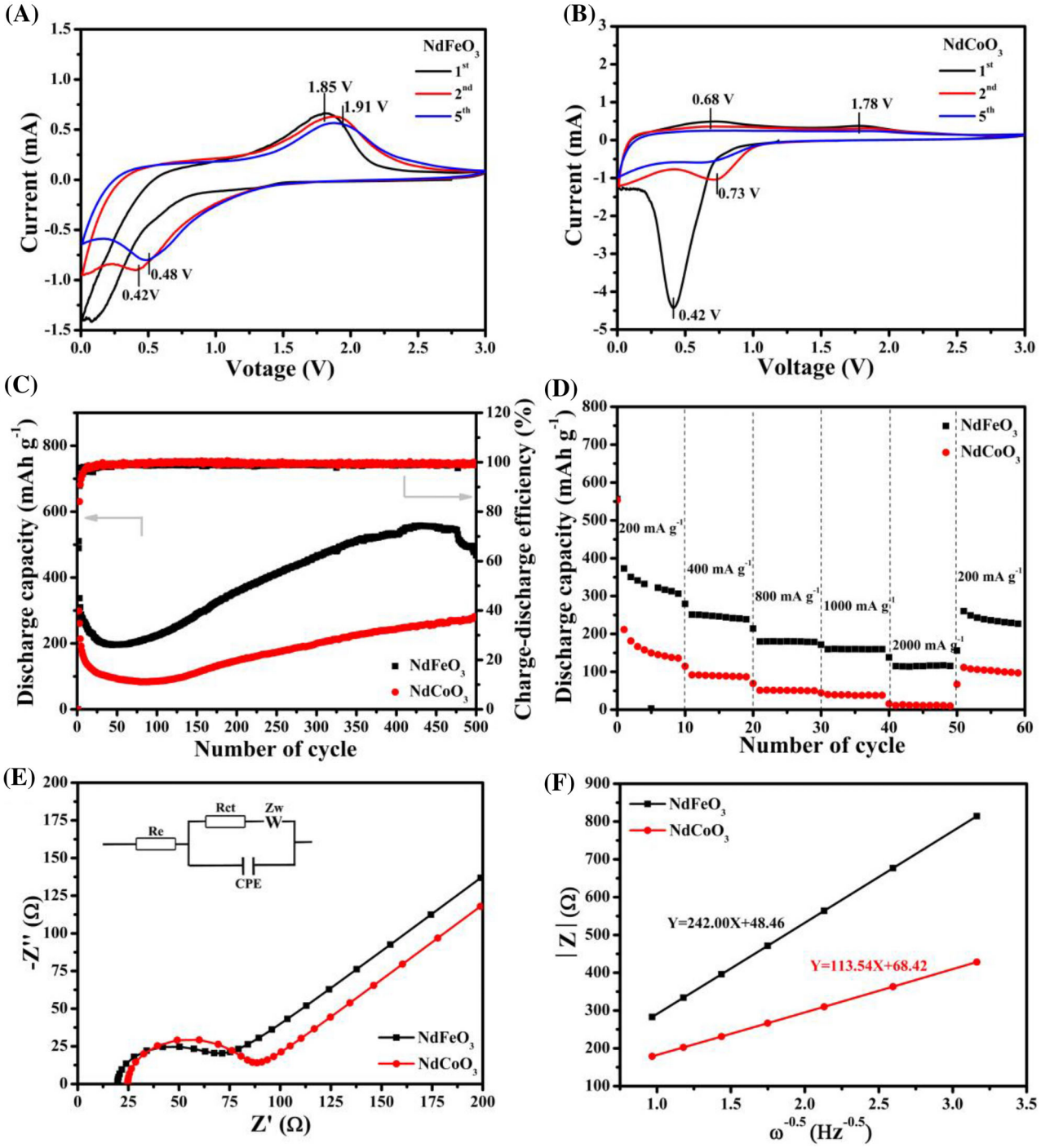

FIGURE 6 *CV* curves of the (A) $NdFeO_3$ nanofibers (NFs) and (B) $NdCoO_3$ NFs for the first, second, and fifth cycles at a scan rate of 0.05 mV s^{-1}; (C) cycle performances of the $NdFeO_3$ and $NdCoO_3$ NFs at 200 mA g^{-1} in the voltage range of 0.01–3.0 V; (D) rate performance of the $NdFeO_3$ and $NdCoO_3$ electrodes; (E) impedance spectra of the $NdFeO_3$ and $NdCoO_3$ NFs at an open-circuit voltage; and (F) fitting line of the $|Z|$ versus $\omega^{-0.5}$ relationship of the $NdFeO_3$ and $NdCoO_3$ NFs

were calculated. The equations are listed in the following equation[53,54]:

$$|Z| = R_s + R_{ct} + \sigma\omega^{-0.5} \quad (6)$$

$$D = \frac{R^2T^2}{2A^2n^4F^4C^2\sigma^2} \quad (7)$$

$$i^{\circ} = \frac{RT}{nFR_{ct}} \quad (8)$$

where ω indicates the angular frequency, R represents the ideal gas constant, n is the transfer charge number, F is the Faraday constant, C signifies the concentration of Li^+ in the electrolyte, and σ is the Warburg coefficient. The corresponding electrochemical impedance parameters of the $NdFeO_3$ and $NdCoO_3$ NFs are listed in Table S7.

The study on the magnetic characteristics of the $NdFeO_3$ and $NdCoO_3$ NFs proved the possible application in the field of condensed matter physics; the research on the electrochemical performance of the $NdFeO_3$ and $NdCoO_3$ NFs as supercapacitor electrodes and Li-ion battery anodes confirmed the practical application in energy storage devices.

4 | CONCLUSIONS

In this work, uniform $NdFeO_3$ and $NdCoO_3$ NFs were fabricated, and elemental mapping images confirmed the homogeneous distribution of Nd, Fe (Co), and O in the $NdFeO_3$ ($NdCoO_3$) NFs. The $NdFeO_3$ NFs present the coexistence of paramagnetic and ferromagnetic states, which were attributed to the magnetization compensation point at low temperature and the noncollinear antiferromagnetic state in the Fe^{3+} subsystem at 298 K. The $NdCoO_3$ NFs exhibited paramagnetic behavior, which was ascribed to the change in electron orbitals. In addition, the particular pseudocapacitive behaviors of $NdFeO_3$ and $NdCoO_3$ were ascribed to the redox reactions of Fe^{3+}/Fe^{2+}, Co^{3+}/Co^{2+}, and $Fe(CN)_6^{3-}/Fe(CN)_6^{4-}$, where the diffusion-controlled process was the dominant charge storage mechanism. At 1 A g^{-1}, the specific capacitances of the $NdFeO_3$ and $NdCoO_3$ NFs were 186.8 and 94.5 F g^{-1}, respectively. As Li-ion battery anodes, at 200 mA g^{-1} the initial specific capacities of the $NdFeO_3$ and $NdCoO_3$ were 337 and 260 mAh g^{-1}, respectively. The $NdFeO_3$ NFs exhibited favorable cycling stability, which was attributed to the reversible valence changes of both Nd and Fe. Thus, the electrochemical performance of the $NdCoO_3$ NFs was ascribed to the multistage electrochemical lithiation process from Co to Co^{2+} to Co^{3+}. This research suggested the feasible applications of the $NdFeO_3$ and $NdCoO_3$ NFs in the field of condensed matter physics and energy storage devices.

ACKNOWLEDGMENTS

This work was financially supported by the Doctoral Scientific Research Foundation of Inner Mongolia Minzu University (Project No: BS437, BS456) and the Research Project of Colleges and Universities in Inner Mongolia Autonomous Region (NJZZ22461). This work was financially supported by the National Natural Science Foundation of China (21961024, 21961025, 22161036), Incentive Funding from the Nano Innovation Institute of Inner Mongolia Minzu University (MDK2019014), and Inner Mongolia Autonomous Region Science & Technology Planning Project for Applied Technology Research and Development (2019GG261).

ORCID

Quanli Hu https://orcid.org/0000-0001-5505-790X

REFERENCES

1. Chen Y, Wang D, Qin H, Zhang H, Zhang Z, Zhou G, et al. CO_2 sensing properties and mechanism of $PrFeO_3$ and $NdFeO_3$ thick film sensor. J Rare Earths. 2019;37:80–7.
2. Chanda S, Saha S, Dutta A, Sinha TP. Raman spectroscopy and dielectric properties of nanoceramic $NdFeO_3$. Mater Res Bull. 2013;48:1688–93.
3. Yuan S, Wang Y, Shao M, Chang F, Kang B, Isikawa Y, et al. Magnetic properties of $NdFeO_3$ single crystal in the spin reorientation region. J Appl Phys. 2011;109:07E141.
4. Dudnikov VA, Orlov YS, Solovyov LA, Vereshchagin SN, Gavrilkin SY, Tsvetkov AY, et al. Effect of multiplicity fluctuation in cobalt ions on crystal structure, magnetic and electrical properties of $NdCoO_3$ and $SmCoO_3$. Molecules. 2020;25:1301.
5. Gildo-Ortiz L, Guillén-Bonilla H, Reyes-Gómez J, Rodríguez-Betancourtt VM, de la L Olvera-Amador M, Eguía-Eguía SI, et al. Facile synthesis, microstructure, and gas sensing properties of $NdCoO_3$ nanoparticles. J Nanomater. 2017;2017:1–10.
6. Chen T, Shen L, Liu F, Zhu W, Zhang Q, Chu X. $NdFeO_3$ as anode materials for S/O_2 solid oxide fuel cells. J Rare Earths. 2012;30:1138–41.
7. Wu Z, Zhang R, Zhao M, Fang S, Han Z, Hu J, et al. Effect of Pd doping on the acetone-sensing properties of $NdFeO_3$. Int J Miner Metall Mater. 2012;19:141–5.
8. Abdel-Latif IA, Rahman MM, Khan SB. Neodymium cobalt oxide as a chemical sensor. Results Phys. 2018;8:578–83.
9. Ateia EE, Arman MM, Morsy M. Synthesis, characterization of $NdCoO_3$ perovskite and its uses as humidity sensor. Appl Phys A–Mater. 2019;125:883.
10. Baiker A, Marti PE, Keusch P, Fritsch E, Reller A. Influence of the A-site cation in $ACoO_3$ (A = La, Pr, Nd, and Gd) perovskite-type oxides on catalytic activity for methane combustion. J Catal. 1994;146:268–76.
11. Fabbri E, Pergolesi D, Traversa E. Materials challenges toward proton-conducting oxide fuel cells: a critical review. Chem Soc Rev. 2010;39:4355–69.
12. Zatsiupa AA, Bashkirov LA, Troyanchuk IO, PetrovG S, Galyas AI, Lobanovsky LS, et al. Magnetization, magnetic susceptibility, effective magnetic moment of Fe^{3+} ions in $Bi_{25}FeO_{39}$ ferrite. J Solid State Chem. 2014;212:147–50.
13. Karpinsky DV, Silibin MV, Trukhanov SV, Trukhanov AV, Zhaludkevich AL, Latushka SI, et al. Peculiarities of the crystal structure evolution of $BiFeO_3$–$BaTiO_3$ ceramics across structural phase transitions. Nanomaterials (Basel). 2020;10:801.

14. Vinnik DA, Zhivulin VE, Uchaev DA, Gudkova SA, Zhivulin DE, Starikov AY, et al. Effect of titanium substitution and temperature variation on structure and magnetic state of barium hexaferrites. J Alloys Compd. 2021;859:158365.
15. Turchenko VA, Trukhanov SV, Kostishin VG, Damay F, Porcher F, Klygach DS, et al. Impact of In^{3+} cations on structure and electromagnetic state of M-type hexaferrites. J Energy Chem. 2022;69:667–76.
16. Turchenko V, Kostishyn VG, Trukhanov S, Damay F, Porcher F, Balasoiu M, et al. Crystal and magnetic structures, magnetic and ferroelectric properties of strontium ferrite partially substituted with In ions. J Alloys Compd. 2020;821:153412.
17. Turchenko V, Kostishin VG, Trukhanov S, Damay F, Balasoiu M, Bozzo B, et al. Structural features, magnetic and ferroelectric properties of $SrFe_{10.8}In_{1.2}O_{19}$ compound. Mater Res Bull. 2021;138:111236.
18. Yuan SJ, Ren W, Hong F, Wang YB, Zhang JC, Bellaiche L, et al. Spin switching and magnetization reversal in single-crystal $NdFeO_3$. Phys Rev B. 2012;87:184405.
19. Ali Z, Ahmad I, Amin B, Maqbool M, Murtaza G, Khan I, et al. Theoretical studies of structure and magnetic properties of cubic perovskite $PrCoO_3$ and $NdCoO_3$. Physica B. 2011;406:3800–4.
20. Turchenko VA, Trukhanov SV, Kostishin VG, Damay F, Porcher F, Klygach DS, et al. Features of structure, magnetic state and electrodynamic performance of $SrFe_{12-x}In_xO_{19}$. Sci Rep. 2021;11:18342.
21. Trukhanov SV, Lobanovski LS, Bushinsky MV, Troyanchuk IO, Szymczak H. Magnetic phase transitions in the anion-deficient $La_{1-x}Ba_xMnO_{3-x/2}$ ($0 \le x \le 0.50$) manganites. J Phys Condens Matter. 2003;15:1783–95.
22. Trukhanov SV, Lobanovski LS, Bushinsky MV, Khomchenko VA, Pushkarev NV, Tyoyanchuk IO, et al. Influence of oxygen vacancies on the magnetic and electrical properties of $La_{1-x}Sr_xMnO_{3-x/2}$ manganites. Eur Phys J B. 2004;42:51–61.
23. Tao L, Da P, Zheng X, Ge B, Hu Z, Wu M, et al. Atomic-level structure engineering of metal oxides for high-rate oxygen intercalation pseudocapacitance. Sci Adv. 2018;4:eaau6261.
24. Shang H, Zuo Z, Liang L, Wang F, Liu H, Li Y, et al. Ultrathin graphdiyne nanosheet grown in situ on copper nanowires and their performance as lithium-ion battery anodes. Angew Chem Int Ed. 2018;57:774–778.
25. Tugova E, Yastrebov S, Karpov O, Smith R. $NdFeO_3$ nanocrystals under glycine nitrate combustion formation. J Cryst Growth. 2017;467:88–92.
26. Yang Y, Feng S, Kan X, Lv Q, Trukhanov AV, Trukhanov SV. Synthesis, Magnetic and electrical characteristics of Ba-Sr hexaferrites substituted with samarium, chromium and aluminum. ChemistrySelect. 2021;6:470–9.
27. Thakur A, Sharma N, Bhatti M, Sharma M, Trukhanov AV, Trukhanov SV, et al. Synthesis of barium ferrite nanoparticles using rhizome extract of *Acorus calamus*: characterization and its efficacy against different plant phytopathogenic fungi. Nano-Struct Nano-Objects. 2020;24:100599.
28. Ge Y, Ul Hoque MdI, Qu Q. 1D Hematite-[α-Fe_2O_3]-nanorods prepared by green fabrication for supercapacitor electrodes. Electrochem Energy Technol. 2019;5:1–6.
29. Lu X, Wang C, Favier F, Pinna N. Electrospun nanomaterials for supercapacitor electrodes: designed architectures and electrochemical performance. Adv Energy Mater. 2016;7:1601301.
30. Wang Y, Yan X, Chen J, Deng J, Yu R, Xing X. Shape controllable synthesis of $NdFeO_3$ micro single crystals by a hydrothermal route. CrystEngComm. 2014;16:858–62.
31. Han R, Dong S, Wang Y, Li X, Zhang Y. Electrical and oxygen sensing properties of $Nd_{1-x}Ba_xCoO_3$ ceramics. J Mater Sci – Mater Electron. 2017;28:14234–9.
32. Dudric R, Bortnic R, Souca G, Ciceo-Lucacel R, Stiufiuc R, Tetean R. XPS on $Nd_{0.6-x}Bi_xSr_{0.4}MnO_3$ nano powders. Appl Surf Sci. 2019;487:17–21.
33. Zhang Y, Ding J, Xu W, Wang M, Shao R, Sun Y, et al. Mesoporous $LaFeO_3$ perovskite derived from MOF gel for all-solid-state symmetric supercapacitors. Chem Eng J. 2020;386:124030.
34. Sasmal A, Sen S, Sujatha Devi P. Synthesis and characterization of $SmFeO_3$ and its effect on the electrical and energy storage properties of PVDF. Mater Res Bull. 2020;130:110941.
35. Liu L, Lang J, Zhang P, Hu B, Yan X. Facile synthesis of Fe_2O_3 nano-dots@nitrogen-doped graphene for supercapacitor electrode with ultralong cycle life in KOH electrolyte. ACS Appl Mater Inter. 2016;8:9335–44.
36. Tian H, Lang X, Nan H, An P, Zhang W, Hu X, et al. Nanosheet-assembled $LaMnO_3$@$NiCo_2O_4$ nanoarchitecture growth on Ni foam for high power density supercapacitors. Electrochim Acta. 2019;318:651–9.
37. Gao C, Zhang P, Xu B, Chen Z, Qi L, Zhang C, et al. Nonvolatile bipolar resistive switching behavior of epitaxial $NdFeO_3$-$PbTiO_3$ thin films grown on Nb:$SrTiO_3$ (001) substrate. Appl Phys Express. 2015;8:051102.
38. Panfilov AS, Grechnev GE, Lyogenkaya AA, Pashchenko VA, Zhuravleva IP, Vasylechko LO, et al. Magnetic properties of $RCoO_3$ cobaltites (R = La, Pr, Nd, Sm, Eu). Effects of hydrostatic and chemical pressure. Physica B. 2019;553:80–7.
39. Vinnik DA, Starikov AY, Zhivulin VE, Astapovich KA, Turchenko VA, Zubar TI, et al. Changes in structure, magnetization and resistivity of $BaFe_{12-x}Ti_xO_{19}$. ACS Appl Electron Mater. 2021;3:1583–93.
40. Troyanchuk IO, Khalyavin DD, Trukhanov SV, Chobot GN. Effect of oxygen content on the magnetic state of $La_{0.5}Ca_{0.5}MnO_{3-\gamma}$ perovskites. J Exp Theor Phys Lett. 1999;70:590–4.
41. Troyanchuk IO, Trukhanov SV, Szymczak H, Przewoznik J, Bärner K. Phase transitions in $La_{1-x}Ca_xMnO_{3-x/2}$ manganites. J Exp Theor Phys. 2001;93:161–7.
42. Trukhanov SV, Lobanovski LS, Bushinsky MV, Fedotova VV, Troyanchuk IO, Trukhanov AV, et al. Study of A-site ordered $PrBaMn_2O_{6-\delta}$ manganite properties depending on the treatment conditions. J Phys Condens Matter. 2005;17:6495–506.
43. Trukhanov SV, Trukhanov AV, Szymczak H, Botez CE, Adair A. Magnetotransport properties and mechanism of the A-site ordering in the Nd-Ba optimal-doped manganites. J Low Temp Phys. 2007;149:185–99.
44. Kumar M, Yun J, Bhatt V, Singh B, Kim J, Kim J, et al. Role of Ce^{3+} valence state and surface oxygen vacancies on enhanced electrochemical performance of single step solvothermally synthesized CeO_2 nanoparticles. Electrochim Acta. 2018;284:709–20.
45. Song H, Fu J, Ding K, Huang C, Wu K, Zhang X, et al. Flexible Nb_2O_5 nanowires/graphene film electrode for high

performance hybrid Li-ion supercapacitors. J Power Sources. 2016;328:599–606.
46. Zhang M, Liu H, Song Z, Ma T, Xie J. Self-assembling $NiCo_2S_4$ nanorods arrays and T-Nb_2O_5 nanosheets/three-dimensional nitrogen-doped garphene hybrid nanoarchitectures for advanced asymmetric supercapacitor. Chem Eng J. 2020;392:123669.
47. Zhang J, Zhang H, Zhang Y, Zhang J, He H, Zhang X, et al. Unveiling of the energy storage mechanisms of multi-modified (Nb_2O_5@C)/rGO nanoarrays as anode for high voltage supercapacitors with formulated ionic liquid electrolytes. Electrochim Acta. 2019;313:532–43.
48. Chen Y, Yan Y, Liu X, Zhao Y, Wu X, Zhou J, et al. Porous Si/Fe_2O_3 dual network anode for lithium-ion battery application. Nanomaterials. 2020;10:2331.
49. Zhu W, Wang Y, Yu Y, Hu Y, Chen Y. Core-shell structured α-Fe_2O_3@$Li_4Ti_5O_{12}$ composite as anode materials for high-performance lithium-ion batteries. J Alloys Compd. 2020;831:152175.
50. Yang Q, Feng C, Liu J, Guo Z. Synthesis of porous Co_3O_4/C nanoparticles as anode for Li-ion battery application. Appl Surf Sci. 2018;443:401–6.
51. Liu H, Le Q. Synthesis and performance of cerium oxide as anode materials for lithium ion batteries by a chemical precipitation method. J Alloys Compd. 2016;669:1–7.
52. Fan L, Zhang W, Zhu S, Lu Y. Enhanced lithium storage capability in Li-ion batteries via porous 3D Co_3O_4 nanofiber anode. Ind Eng Chem Res. 2017;56:2046–53.
53. Hua C, Fang X, Wang Z, Chen L. Lithium storage in perovskite lithium lanthanum titanate. Electrochem Commun. 2013;32:5–8.
54. Gao Y, Wang X, Yu W, Liu G, Dong X, Wang J. Construction of $LiMn_2O_4$ microcubes and spheres via the control of the (104) crystal planes of $MnCO_3$ for high rate Li-ions batteries. RSC Adv. 2019;9:21009–17.

SUPPORTING INFORMATION

Additional supporting information can be found online in the Supporting Information section at the end of this article.

How to cite this article: Hu Q, Yue B, Su W, Yang D, Wang Y, Dong X, et al. Syntheses, characterization, magnetic, and electrochemical properties of perovskite-type $NdFeO_3$ and $NdCoO_3$ nanofibers. J Am Ceram Soc. 2022;1–12. https://doi.org/10.1111/jace.18648